Hydrogel composites based on chitosan and CuAuTiO$_2$ photocatalysts for hydrogen production under simulated sunlight irradiation

Oscar Ramírez [a], Antón Lopéz-Frances [b], Herme G. Baldoví [b], César Saldías [a], Sergio Navalón [b], Angel Leiva [a], David Díaz Díaz [c,d,*]

[a] *Facultad de Química y de Farmacia, Pontificia Universidad Católica de Chile, Santiago 7820436, Chile*
[b] *Departamento de Química, Universitat Politècnica de València, Camino de Vera s/n, Valencia 46022, Spain*
[c] *Departamento de Química Orgánica, Universidad de la Laguna, La Laguna 38206, Spain*
[d] *Instituto Universitario de Bio-Orgánica, Universidad de la Laguna, La Laguna 38206, Spain*

ARTICLE INFO

ABSTRACT

This study explored the photocatalytic hydrogen evolution reaction (HER) using novel biohydrogel composites comprising chitosan, and a photocatalyst consisting in TiO$_2$ P25 decorated with Au and/or Cu mono- and bimetallic nanoparticles (NPs) to boost its optical and catalytic properties. Low loads of Cu and Au (1 mol%) were incorporated onto TiO$_2$ via a green photodeposition methodology. Characterization techniques confirmed the incorporation of decoration metals as well as improvements in the light absorption properties in the visible light interval ($\lambda > 390$ nm) and electron transfer capability of the semiconductors. Thereafter, Au and/or Cu NP-supported TiO$_2$ were incorporated into chitosan-based physically crosslinked hydrogels revealing significant interactions between chitosan functional groups (hydroxyls, amines and amides) with the NPs to ensure its encapsulation. These materials were evaluated as photocatalysts for the HER using water and methanol mixtures under simulated sunlight and visible light irradiation. Sample CuAuTiO$_2$/ChTPP exhibited a maximum hydrogen generation of 1790 μmol g^{-1} h^{-1} under simulated sunlight irradiation, almost 12-folds higher compared with TiO$_2$/ChTPP. Also, the nanocomposites revealed a similar tendency under visible light with a maximum hydrogen production of 590 μmol g^{-1} h^{-1}. These results agree with the efficiency of photoinduced charge separation revealed by transient photocurrent and EIS.

1. Introduction

The current growing energy demands of society are supported mainly by the combustion of fossil fuels (i.e., oil, coal and natural gas). This situation would imply in the mid- and long-term future a depletion of fossil fuels with concomitant emission of carbon dioxide (CO$_2$) to the atmosphere, since currently, CO$_2$ is recognized as the main anthropogenic greenhouse gas responsible for climate change. For these reasons, the urgent development of alternative energy vectors from sustainable resources [1,2] is scientifically recognized. Therefore, important efforts have been made to develop novel, efficient and cost–effective technologies to address the production and storage of energy, such as the scientific progress in the energy field, regarding the development of photovoltaic devices [3] and new generation lithium-ion batteries [4].

In this context, molecular hydrogen (H$_2$) is considered as a promising fuel for several reasons, such as its unique ability to store large amounts of energy and its ideal energy release with water as the only byproduct of the reaction [5,6]. However, currently, hydrogen production at the industrial scale is carried out mainly by the steam–methane reforming reaction, a process associated with several significant drawbacks, such as the large energy requirements, notable CO$_2$ emissions and dependence on hydrocarbon sources. Because of the above, the use of hydrogen produced by this pathway does not have a considerable impact on energetic and environmental matters, and are motifs for the constant efforts made to replace fossil starting materials with more sustainable sources [7] and on the incorporation of adsorbents to mitigate carbon emissions [8] are constantly being explored. For these reasons, other cleaner and energetically efficient routes for the synthesis of hydrogen have been investigated.

In a pioneering study, Fujishima and Honda [9] reported the use of TiO$_2$ photoelectrodes for the water splitting reaction and opened a research front in the area of photo(electro)catalytic hydrogen

---

generation. This process consists of irradiating semiconductor materials such as TiO_2 nanoparticles (NPs) with appropriate energy, after which excited electrons are transferred from the valence to the conduction band, while photogenerated holes are left in the valence band. After electron-hole pairs migrate to the solid surface, reduction, and oxidation reactions, such as H_2O decomposition into H_2 and O_2, respectively, can occur [10–12]. Nevertheless, TiO_2 requires UV light ($\lambda < 390$ nm) to afford its photoexcitation and promote the generation of hydrogen molecules, property attributed to its wide band gap (3.2 eV). This situation hampers the efficient use of solar light irradiation since the proportion of UV light reaching the Earth's surface is only 4–5 % [13]. In addition to the previous, the fast recombination of photogenerated electrons and holes in the bulk of the semiconductor, reverse reaction, has reaction rates of several orders of magnitude higher than their formation, and is another relevant limitation to be considered when attempting to increase the efficiency of the photocatalytic process [14,15]. To overcome these issues, several strategies are in constant development to attain more efficient photocatalytic systems. Among them, decoration of TiO_2 with metal NPs such as Pt [16] and Pd [17], which can act as electron traps, is a successful strategy to partially avoid charge carrier recombination and thus increase the overall efficiency of the photocatalytic process [18], strategy with remarkable ability to be applied also for the degradation of other organic compounds for environmental remediation applications [19]. In addition, the modification of TiO_2 with plasmonic metal NPs such as Au [20] and Ag [21] also favors visible light absorption by the photocatalyst, with maximum absorption bands located at approximately 530 and 420 nm, respectively, given their localized surface plasmon resonance (LSPR) effect, a property that is added to the decrease in the recombination of photogenerated species. It should be noted that the LSPR effect of metal NPs depends on their structural morphology, such as their size and shape, as well as the properties of their surroundings (i.e., dielectric media) [22]. This property has the potential to allow decorated semiconducting materials to take advantage of the visible portion of solar light that reaches the earth's surface which is an appreciated source of energy, since it represent approximately 43 % of the total solar light that passes through the atmosphere. Despite these comments, decorating semiconducting materials with noble metals hampers their wide application due to their scarcity and high cost. For that reason, the use of other earth-abundant plasmonic metals, such as Cu–based NPs, to decorate semiconductor surfaces is gaining increasing attention as a cost-efficient strategy. Interestingly, it has been demonstrated that Cu(0) NPs exhibit a light absorption band in the visible region due to LSPR phenomena, usually centered at approximately 600 nm [23], with high relevancy to improve the photocatalytic behavior of some semiconducting materials by its surface deposition [24]. However, metallic Cu NPs can be oxidized to some extent to copper oxide NPs, thus reducing their ability to absorb visible light due to the LSPR effect. Because of the previous, strategies to avoid the oxidation of Cu(0) nanostructures are in growing develop, such as for example, the use of organic capping agents to limit the contact of Cu atoms with oxidizing agents but also with reactants. On the other hand, recent studies have demonstrated that the formation of alloyed NPs of Cu with noble metals permits the stabilization of metallic copper species, avoiding its oxidation and preserving its metallic state [25]. In addition, this strategy not only improved the stability of Cu structures during oxidation but also boosted their photocatalytic activity, as reported by Chen and coworkers, who demonstrated the enhanced performance of CuAu alloyed nanosystems for the photodegradation of RhB under simulated light irradiation [26], in which the combination of both metals is key for the appearance of boosted catalytic properties and also allowing the tuning of its optical properties [27,28]. It is important to remark the potential of similar systems to be applied in other environmental remediation technologies as reported in the literature [29,30].

In addition to the interesting and improved properties shown by semiconducting materials decorated with metal NPs, the use of supporting materials of different natures can affect and tune the activity of these systems, mostly due to strong interactions with the support [31,32]. Moreover, the use of polymers has attracted considerable interest in this field, first, to promote the stability of these systems while avoiding spontaneous agglomeration and second, to promote close interactions with the surface of these nanosystems. In this regard, a wide variety of synthetic polymers have been employed for hydrogen generation applications [33–35]. However, the extensive use of synthetic polymers, associated with oil and nonrenewable sources, with poor degradation over time, has led to the accumulation of large amounts of waste in landfills, generating major concerns about the use of plastics and the presence of microplastics in nature [36]. For that reason, the use of biopolymers in several areas has gained considerable attention, mainly because biopolymers are renewable resources abundantly found in nature with faster generation periods, a wide diversity of chemical structures and the presence of functional groups; thus, biopolymers can be applied mostly in fields such as tissue engineering [37] and packaging [38]. A particular biopolymer to consider with great availability and, for that reason, low cost is chitosan, a biopolymer obtained by the deacetylation of chitin, a biopolymer found in the exoskeleton of several crustaceous species, and which can also be produced in bioreactors by some fungi [39]. Furthermore, the great attractive of chitosan-based technologies relapses on its potential to be obtained in large scales from wastes, especially from some marine industries, and also to be applied in waste treatment applications with other marine resources [40,41]. In addition, chitosan has been identified as a remarkable resource in several fields, serving as a suitable starting material for attaining the aspects of sustainable development and circular economy stated in sustainable development goals (SDGs) [42], gaining considerable attention for use in the synthesis and stabilization of different nanostructured systems because of the strong interactions between chitosan functional groups and the surfaces of different nanoagents [43]. Considering these findings, chitosan hydrophilic functional groups are likely to interact with the surface of modified semiconducting NPs [44], a phenomenon that might also favor water splitting in two senses: first, favoring the rapid availability of water molecules near the surface of the NPs due to the hydrophilic character of the matrix; second, the presence of hole–scavenging species to promote hydrogen generation due to the presence of alcohol groups that can act as sacrificial electron donors and partially avoid electron-hole recombination; appealing aspects in the field of hydrogen generation catalysts that has been stated to serve as an energy saving way of producing hydrogen [45].

With these precedents, the aim of this work was to develop three novel hydrogels nanocomposites containing chitosan and TiO_2 decorated with plasmonic Cu and Au-based NPs to be used as photocatalysts for the hydrogen evolution reaction (HER). Initially, Au and Cu mono- and bimetallic NPs were deposited onto TiO_2 by a photodeposition method, and as a way to improve the photogeneration of charge carries, enable the absorption of visible light and to reduce the recombination of photoexcited species. The improvements in the photoelectronic behavior of the materials were characterized by transient photocurrent and electrochemical impedance spectroscopy measurements using Cu- and Au NP-supported TiO_2. The resulting solids were subsequently incorporated into chitosan hydrogels through physical crosslinking of chitosan chains with sodium tripolyphosphate molecules, obtaining a material denominated ChTPP. Finally, the composites were evaluated as photocatalysts for the HER under both simulated and solar visible light irradiation.

2. Experimental section

2.1. Materials

Titanium dioxide P25 Degussa NPs (TiO_2, Sigma–Aldrich, 99.5 %), potassium gold (III) chloride ($KAuCl_4$, Sigma–Aldrich, 99.995 %), copper (II) chloride dihydrate ($CuCl_2 \times 2H_2O$, Merck, 99.9 %), methanol

(MeOH, Sigma–Aldrich, 98 %), high-molecular-weight chitosan (Ch, Sigma–Aldrich, ~160 kDa, DD > 75 %), glacial acetic acid (HAc, Merck, 99.5 %), NaTPP (Sigma–Aldrich, 85 %). All reagents were used as received without further purification. Distilled water was used in all the experiments unless otherwise stated.

2.2. Photochemical synthesis of metallic NPs supported on TiO₂ (MTiO₂)

Metallic NPs were synthesized on the surface of TiO_2 by modifying a previous route reported by Chen and coworkers [46]. First, 100 mg of TiO_2 was dispersed in 40 mL of methanol inside a round bottom flask by successive cycles of magnetic stirring and ultrasound bath sonication. Subsequently, 24 mM $KAuCl_4$ and 73 mM $CuCl_2 \times 2H_2O$ aqueous solutions were added to the previous dispersion to achieve a theoretical loading of 1 mol% on TiO_2. The aliquots used to prepare each mono– and bimetallic sample are listed in SI 1. The adsorption of metal ions on TiO_2 was maintained with magnetic stirring at 700 rpm and 40 °C for 1 h. After that, the dispersions were cooled to room temperature and transferred to a conventional Rayonet photoreactor provided with 8 UV lamps with an emission wavelength of 254 nm (6 watts each) for 1 h to promote photoreduction of the adsorbed metals. After that, the dispersion was removed from the photoreactor, centrifuged, and washed three times with water and one with ethanol. Finally, the decorated TiO_2 was dried in a vacuum oven at 60 °C for 12 h and stored prior to use. These systems were denoted as $MTiO_2$, where M indicates the decoration with Cu and/or Au.

2.3. Encapsulation of MTiO₂ inside chitosan hydrogels

The incorporation of TiO_2 and $MTiO_2$ NPs into chitosan–based hydrogels was carried out by mixing an aqueous dispersion of the NPs with a chitosan solution. For this purpose, chitosan was first dissolved in an HAc solution (1.25 % *v/v*) to obtain a chitosan concentration of 1.25 % *w/v*; this mixture was stirred overnight to properly dissolve the chitosan powder. In parallel, a 15 mg/mL aqueous dispersion of TiO_2 and/ or $MTiO_2$ was prepared with the help of an ultrasound bath. Then, 2 mL of the NP dispersion was added to 8 mL of the chitosan solution, which was stirred *vigorously* at room temperature for 1 h. Subsequently, the mixture was transferred to a syringe provided with a G25 needle, and the solution was slowly added dropwise at a rate of 0.3 mL/h to 50 mL of a 1 % *w/v* NaTPP solution. As drops of the solution were added to the NaTPP solution, chitosan hydrogel beads, referred to as ChTPP, started to appear, and the NPs started to color the gels. After the complete addition of the chitosan solution, the beads were left for 1 h immersed in the NaTPP bath. Finally, the solutions were washed three times with water and then lyophilized prior to characterization and evaluation as catalysts.

2.4. Photocatalytic testing

Photocatalytic HER of the hydrogel nanocomposites was carried out in a 50 mL glass reactor equipped with two stainless steel connections, one provided with a needle for the entrance of the purge gases and one with a manometer to measure the internal pressure of the system and details can be found elsewhere [47]. The photocatalytic activities of the different composites were quantitatively compared by using the same amount of solid as photocatalyst and maintaining the other reaction conditions constant. In a typical experiment, 5 mg of a lyophilized nanocomposite was immersed in 10 mL of a MeOH/water 1:4 solution. For comparison, some experiments were carried out using 10 mL of water in absence of methanol. Immediately after, the system was sealed and purged with argon for 15 min, degasified with an ultrasound bath (450 W) for 15 min, and finally pressurized with argon at approximately 1 atm by using a manometer coupled to the reactor. Then, the system was irradiated (Hg – Xe 150 W lamp equipped with an A10014–50–0110 optical fiber) with simulated sunlight (AM 1.5G; 236 mW/cm²) or

visible light (λ > 420 nm; 272 mW/cm²) for 1 h, irradiances were measured by using a commercially available photodiode (843-R Optical power meter; Newport Corporation). The temperature of the reaction monitored during the photocatalytic experiments by using an infrared thermometer was found to be 35 °C. Reaction aliquots of evolved gases at different reaction times were analyzed using an Agilent 490 MicroGC system equipped with a Molsieve 5 Å column. Control experiments without NPs, nanocomposites and only polymeric beads were conducted showing no detectable hydrogen generation under both irradiation conditions.

2.5. Characterization techniques

HRTEM images were obtained using a TALOS F200C G2 instrument with an acceleration voltage of 200 kV. The samples were previously dispersed in MeOH, sonicated for 10 min, supported on copper grids by dropping a few microliters of sample, and then dried in a vacuum oven overnight before analysis. Image analysis was carried out using ImageJ software, in which the average NP size was obtained by measuring at least 150 nanoentities. ICP–OES measurements were performed to determine the amount of metal deposited on the materials. These analyses were performed in an ICP–OES AVI500 Perkin Elmer spectrophotometer, and the quantification of the metallic content was determined by a calibration curve that ranged from 8 to 100 ppb (detection limit of 5 ppb) for Au and from 8 to 72 ppb (detection limit of 3 ppb) for Cu. FESEM images were obtained using a QUANTA FEG 250 instrument with an accelerating voltage of 30.0 kV. Moreover, an Oxford X–Max50 detector was used for the EDX spectroscopy analysis in mapping mode. Image processing of the FESEM and EDX maps was conducted using ImageJ and Origin software, respectively. XRD diffractograms were recorded using a Panalytical Empyrean diffractometer equipped with a copper anode using kα 1 and 2 as the irradiation source. The measurements consisted of scanning from 5 to 80° 2θ, with a path of 0.0263° and a measurement time of 60 s per angle. UV–Vis spectroscopy was performed with a Cary–60 UV–Vis spectrophotometer. Measurements were made in quartz cuvettes of 1 mL with an optic path of 1 cm. The NPs were dispersed in water and measured between 200 and 800 nm with an appropriate scanning rate. Diffuse reflectance UV–vis spectroscopy (DRS) was recorded in a Cary 5000 Varian spectrophotometer having an integrating sphere. Electrochemical impedance spectroscopy (EIS) and photocurrent measurements were carried out using a Gamry Instruments potentiostat (model Interface 5000E) as previously reported [48].The simplified Randless equivalent circuit used to fit each EIS spectrum and calculate the charge transfer resistance (R_{ct}), series resistance (R_s) and double-layer capacitance (C_{dl}), is shown in SI 2. Briefly, $CuAuTiO_2$, $AuTiO_2$ or TiO_2 were supported on a carbon electrode that was used as the working electrode and polarized at +0.9 *V*. The experiments were performed using a standard three-electrode configuration containing a deoxygenated $TBAPF_6$ (0.1 M) acetonitrile solution in the presence of methanol (0.3 mL). TGA was employed to characterize the thermal stability of the materials. For that purpose, the samples were measured with a Mettler–Toledo TGA/SDTA851 thermobalance. The TGA profiles were analyzed under a nitrogen flow of 20 mL min⁻¹ and from 25 to 900 °C with a heating rate of 10 °C min⁻¹. The data were processed using STARe software version 8.1. FT–IR spectra were recorded with a PerkinElmer UATR spectrophotometer, which was obtained with an ATR sample–holder. The direct insertion of the lyophilized hydrogels and nanocomposites into the ATR probe was analyzed, and the results were measured between 4000 and 400 cm⁻¹, with a resolution of 1 cm⁻¹ and an accumulation of 32 scans per sample. The photogenerated gases were detected and quantified by an Agilent μGC 490 instrument equipped with a column filled with 5 Å molecular sieves and Ar as the mobile phase.

3. Results and discussion

Initially, TiO$_2$-supported plasmonic Au and Cu NPs were synthesized by the photodeposition method, Fig. 1. This method consists of UV irradiation of a TiO$_2$ suspension in a mixture of water and methanol containing a metal salt precursor under argon conditions. In this process, photogenerated electrons are responsible for metal salt reduction to metal NPs, while holes oxidize methanol to serve as sacrificial electron donors [49,50], strategy that has been pointed as an efficient way for energy savings, especially for hydrogen production. Attempts to recover Cu NP-supported TiO$_2$ under ambient conditions result in rapid decoloration of the material under air, SI 3; thus, this material was not further considered in this study.

Subsequently, TiO$_2$ surface modification with Au and CuAu NPs was confirmed by electron microscopy, Fig. 2. SEM images, Fig. 2a and d, showed the presence of agglomerates associated with TiO$_2$ particles decorated with Au or CuAu NPs. In addition, STEM measurements revealed the presence of dark spots attributed to the presence of Au and CuAu NPs supported on TiO$_2$, Fig. 2b and e. These samples were also analyzed by HRTEM, again revealing the presence of nanostructures with different electronic contrasts, suggesting the presence of Au and CuAu supported on TiO$_2$; these structures had irregular morphologies with average particle diameters of 22.3 and 14.1 nm, respectively, Fig. 2c and f. EDX elemental mapping analysis of CuAuTiO$_2$ further confirmed the presence of Au and Cu within the same particle and thus confirmed the formation of CuAu alloy NPs supported on TiO$_2$.

To confirm the presence of Au and Cu NPs on TiO$_2$ and to determine the composition of the material, the materials were analyzed via ICP–OES, revealing the presence of both metals, which were found in molar compositions of approximately 1.2 and 0.8 mol% for AuTiO$_2$ and CuAuTiO$_2$, respectively. Moreover, for the sample decorated with bimetallic NPs and CuAuTiO$_2$, the molar ratio between the Cu and Au atoms was approximately 1.32. Additionally, the decorated nanoparticles were analyzed via EDX coupled with FE–SEM to observe the presence of Cu and Au metals on the nanoparticles in the CuAuTiO$_2$ sample. Fig. 3a shows an image of the CuAuTiO$_2$ sample in which an EDX mapping was obtained from a portion of the image, revealing the presence of Ti, O, Au and Cu atoms in Fig. 3b, c, d and e, respectively. These EDX measurements suggest the formation of Cu and Au alloys supported on TiO$_2$. Added to the above, HRTEM characterization of AuTiO$_2$ revealed that the observed dark spots with d-spacing values of 0.235 nm characteristic of the (111) facets of Au NPs, SI 4. Similarly, the presence of 0.36 nm lattice spacings revealed the presence of (101) facets of TiO$_2$ anatase, SI 4. Complementary, characterization by SEM-EDX by point analysis or elemental mapping further confirmed the chemical nature of these Au or TiO$_2$ NPs, SI 5. In the case of CuAuTiO$_2$ solid, the measured spacing lattice of the fringe from HRTEM analysis was 0.23 nm, SI 6, a value that is between the value of Au (111) facet (0.235 nm) and Cu (111) (0.2087 nm) and associated with the formation of CuAu alloy [51]. Additionally, SEM-EDX analyses confirmed the presence of Au and Cu elements within the same particle in agreement

with the formation of alloy metal NPs, SI 7.

The materials were further analyzed by XRD and UV–Vis spectroscopy, with the aim of studying possible changes in the crystalline structure and optical properties of the materials. Fig. 4a shows the XRD diffractograms of the AuTiO$_2$, CuAuTiO$_2$ and pristine TiO$_2$ samples. The main signals corresponding to the TiO$_2$ crystalline structure were observed and are labeled as peaks (a), (b) and (c), which appear at 25, 27 and 38°, respectively, and are in agreement with the diffraction planes of the anatase phase (101), rutile (100) and a group of signals attributed to diffraction planes of TiO$_2$ such as (103), (004) and (112), respectively. Additionally, for TiO$_2$ decorated with Au, peak (c) is accompanied by signals corresponding to Au crystalline planes (111), confirming the decoration of the semiconductor with this metal, SI 8. The intensities of peaks (a) and (b) were determined following a methodology reported by Spurr and Myers [52] to analyze the proportions of the anatase and rutile phases, SI 9; the results are detailed in Table 1, which shows the anatase and rutile compositions, as well as the crystallite size obtained by the Scherrer equation. As observed, 86.4 % and 13.6 % of the analyzed samples were anatase and rutile, respectively, and exhibited no significant changes over the employed metallic decoration, suggesting that the modification of TiO$_2$ is mostly superficial without relevant alteration of its crystalline structure during photoreduction synthesis. In addition, the crystalline sizes of both phases were calculated by the Scherrer equation, SI 10, and the results revealed sizes of approximately 20.1 ± 0.1 and 25.9 ± 1.7 nm, similar to those observed in the TEM images; these findings were probably attributed to the polymorphic composition of the Degussa P25 TiO$_2$. On the other hand, the optical properties of the samples obtained by DRS, Fig. 4b, depicts an absorption band at 550 nm for the case of the decorated systems, which corresponds to the plasmonic light absorption band of the Au and CuAu-based nanostructures. The optical properties of the materials were further analyzed by Tauc plots, Fig. 4c, revealing considerable changes in the band gap of the semiconductor as decoration metals were incorporated [53]. First, pristine TiO$_2$ showed a band gap at 3.24 eV, which mainly corresponds to the TiO$_2$ anatase phase band gap, given its greater abundance in the material. Then, as Cu and Au atoms are deposited on the semiconducting surface, the band gaps of the different materials start to decrease, reaching values of 3.11 and 3.09 eV for TiO$_2$ decorated with Au and CuAu NPs, respectively. The observed decrease in the band gap of the semiconductor was associated with an increase in the light absorption window of the materials loaded with Au and CuAu NPs in the visible region in agreement with the localized surface plasmon resonance of these metal NPs. Also, it is noteworthy that the optical properties and the band position of these materials are in adequate agreement to carry out the photocatalytic hydrogen production by HER.

To determine the influence of TiO$_2$ decoration with Au or CuAu NPs on photogenerated carriers, several (photo)electrochemical measurements under simulated sunlight irradiation were carried out using pristine TiO$_2$, AuTiO$_2$ (1 %) and CuAuTiO$_2$ (1 %). The transient photocurrent responses of the corresponding FTO electrodes were evaluated using a mixture of acetonitrile and methanol to mimic photocatalytic hydrogen generation from water and methanol mixtures, in which methanol was used as a sacrificial electron donor. The obtained results, Fig. 5a, indicate that CuAuTiO$_2$ exhibits the highest current intensity response, followed by AuTiO$_2$ and pristine TiO$_2$. Electrochemical impedance spectroscopy measurements were also carried out, and the results can be visualized with Nyquist plots, Fig. 5b. The smallest Nyquist arc radius was obtained for the CuAuTiO$_2$ sample, followed by that of AuTiO$_2$ and pristine TiO$_2$. It should be noted that the smallest arc radius of a Nyquist plot corresponds to the sample exhibiting the lowest electric charge transfer resistance. To quantify these EIS results a simplified Randles equivalent circuit, SI 2, was used to fit each spectrum. This Randles circuit is equivalent to an equivalent electrical circuit consisting of a series of resistance (R_s) and double-layer capacitance (C_{dl}). The obtained charge transfer resistance of CuAuTiO$_2$, AuTiO$_2$ and TiO$_2$ were 2175, 3553 and 3914 Ω, respectively. In summary, transient
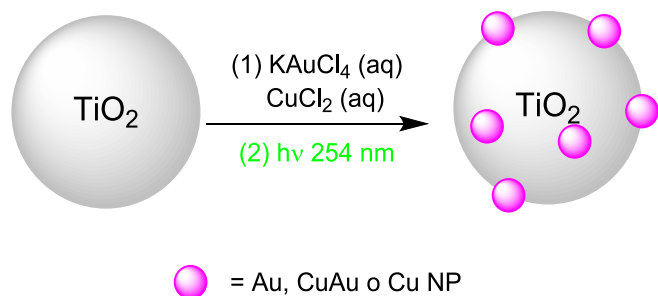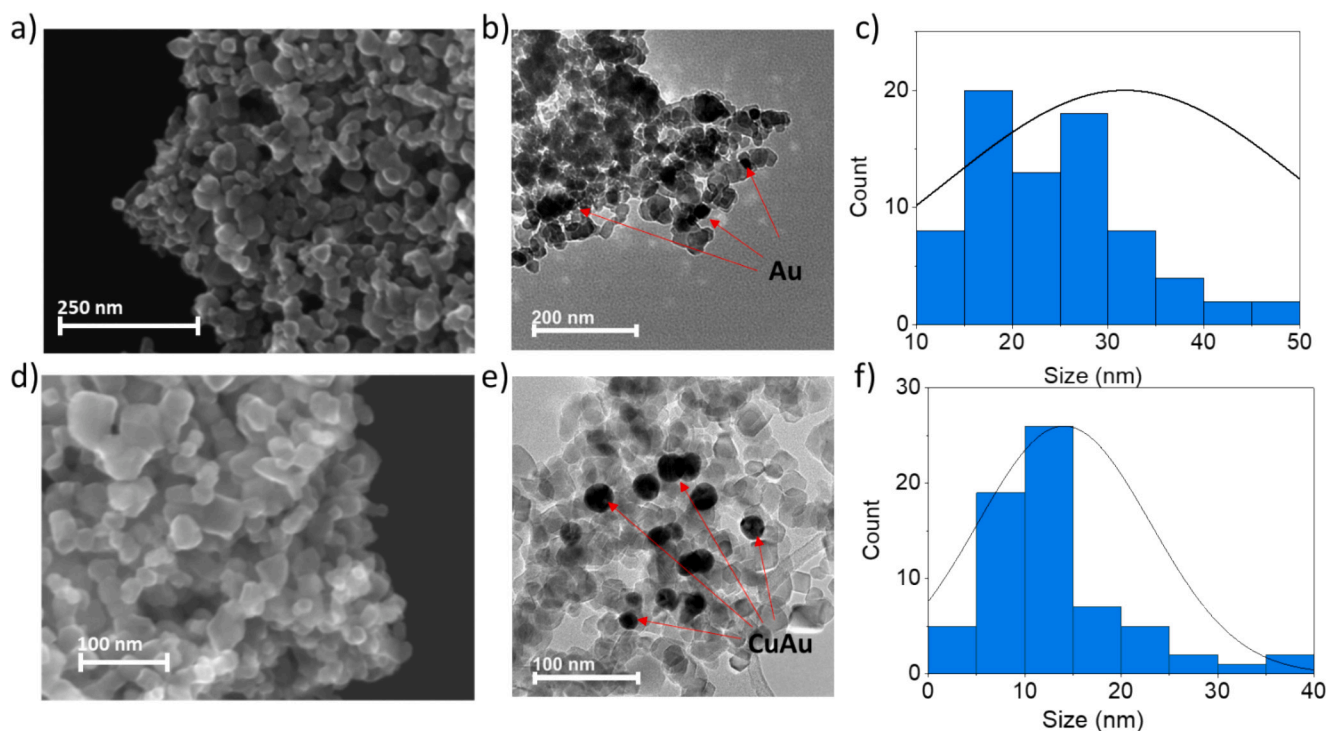

**Fig. 1.** Schematic representation of the surface modification of TiO$_2$ with metal NPs.

Fig. 2. SEM (a, d) and TEM (b, e) images of AuTiO$_2$ (a, b) and CuAuTiO$_2$ (d, e). Panels (c) and (f) contain the Au and CuAu particle size distributions, respectively.

photocurrent measurements and Nyquist plots indicate that the efficiency of photoinduced charge separate and transfer electrons decreases in the order CuAuTiO$_2$ > AuTiO$_2$ > TiO$_2$.

After characterizing the Au- and CuAu-supported TiO$_2$ materials, they were embedded inside chitosan biobased hydrogels, a system that was physically crosslinked by tripolyphosphate molecules, a polyanionic molecule that is able to interact with multiple protonated amino groups present in the chitosan chains to drive the formation of the hydrogel network [54]. The incorporation of decorated TiO$_2$ was initially confirmed by the distinctive purple coloration of the hydrogel due to the presence of the metal NPs, Fig. 6a, obtaining gel beads with average size of 1.46 mm, SI 11; this coloration was not affected after successive washing treatments, initially suggesting a proper stabilization of the NPs by the polymer chains. Subsequently, the thermal properties of the hydrogel nanocomposites were studied by TGA. Fig. 6b shows that the samples had a considerable capacity to swell with water, as indicated by the notable weight loss observed at a maximum degradation rate (T$_{md}$) of 100 °C, which represents approximately 85 % w/w of the ChTPP hydrogel. In addition, a second degradation stage was also possible to detect, with a T$_{md}$ of approximately 294 °C, probably corresponding to the thermal degradation of the chitosan chains that form part of the nanocomposite. Similarly, the thermal degradation profile of the hydrated AuTiO$_2$/ChTPP beads exhibited analogous behavior but with a lower water content, near 80 % w/w, which might indicate the expulsion of water molecules from the hydrogel by the incorporation of NPs to form the composite. Additionally, the second degradation stage was also observed but with a slight shift in the T$_{md}$ to lower temperatures, which might provide insight into the possible interactions between the organic and inorganic portions that form the nanocomposite. In this regard, with the goal of obtaining deeper insight into the composition of the nanocomposite, lyophilized samples of the materials were also analyzed; the results are depicted in Fig. 6c and show two main thermal weight loss stages. The first stage was found with a T$_{md}$ near 100 °C and was assigned to the evaporation of moisture still adsorbed to the polymer network after the lyophilization process. A second stage was subsequently observed with a T$_{md}$ at approximately 302 °C, which was probably ascribed to the degradation of chitosan chains during thermal

analysis, as indicated in previous works [55,56]. On the other hand, despite the presence of the decorated TiO$_2$ embedded in the hydrogels, the thermal degradation profile of the systems containing NPs was similar to that of pristine chitosan prior to the synthesis of the hydrogels, SI 12, and ChTPP lyophilized hydrogels, suggesting that the NPs did not introduce new thermal degradation stages. However, the second degradation step showed a considerable shift in the T$_{md}$ to lower temperatures in the case of the nanocomposites, with a T$_{md}$ of 270 °C, which was clearly observed in the DTG curves of the samples, SI 13, confirming that the thermal properties were modified during the analysis of the hydrated gels. The decrease in the thermal stability of the nanocomposites could be associated with the presence of MTiO$_2$ inside the matrix, in which the NPs could interact with some chitosan functional groups, tending to weaken some chemical bonds in the polymer backbone and facilitating thermal degradation at lower temperatures. In addition, it is important to acknowledge the final amount of residue at the end of the TGA experiment, in which a considerable increase in the number of substances containing NPs was found in comparison with that in pristine ChTPP samples. This residue is probably composed of a mixture of carbonaceous material obtained from the anaerobic calcination of the organic portion of the material that is not able to decompose into small molecules and volatilize [57]; this mixture is accompanied by inorganic NPs, which do not undergo significant thermal decomposition under the employed experimental conditions, as stated previously. Considering the above, the differences in the final residue value could be employed as a way to approximately determine the amount of inorganic material in the composites; difference that seems to be near 20.9 % w/w for the composite and is in close agreement with the nominal value employed during the synthetic procedure to prepare the samples, which is approximately 23 % w/w considering the concentrations of the MTiO$_2$ dispersion and polymer solution, remarking the ability of the ChTPP hydrogels to successfully encapsulate the NPs in its matrix confirmed that the hydrogel could serve as an adequate support for dispersing and transporting the NPs.

The lyophilized hydrogels were also characterized by FT–IR spectroscopy to determine the interactions of the chitosan chains with the MTiO$_2$, Fig. 6d. The spectra of the pristine chitosan beads revealed the
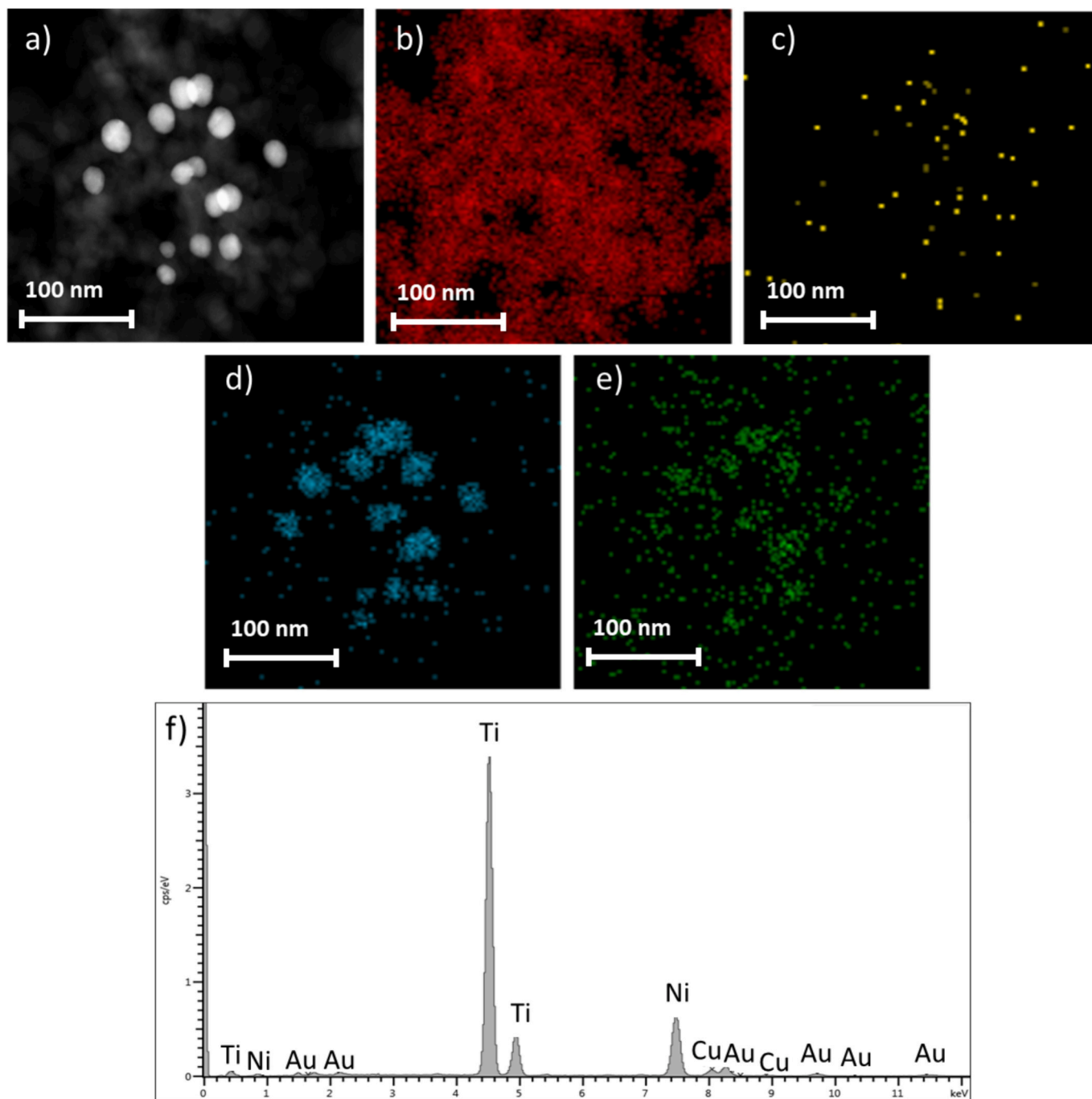
Fig. 3. (a) FESEM image of the CuAuTiO$_2$ sample and EDX mapping for (b) Ti, (c) O, (d) Au and (e) Cu. The corresponding EDX spectrum is shown in panel (f).

presence of the main signals corresponding to the chitosan functional groups, identified as follows: (1) O—H stretching vibration overlapped with N—H stretching vibrational bands at 3200 cm^{-1} and (2) C—H stretching band at 2870 cm^{-1}. Signals (3) and (4) correspond to the vibrational modes of amide functional groups, referred to as amide I and amide II vibrations, respectively, in which the first band appears at 1631 cm^{-1} corresponding to the stretching vibration of C=O groups in the acetylated portions of chitosan, while the second band is attributed to the bending vibration of N—H and C—N bonds, which appears at 1531 cm^{-1}. Afterwards, signal (5) indicates the stretching mode of the P=O present in the TPP crosslinker used to initially form the hydrogels at 1151 cm^{-1}, confirming its role during the synthetic procedure. Finally, the signal (6) at 1057 cm^{-1} indicates the vibrational modes of the C—O and C–O–C bonds of the glycosyl units of chitosan, similar to

previous reports by Zawadzki and Kackzmarek [58]. Then, as the different NPs were incorporated to form the nanocomposites, the main signals attributed to the chitosan support were still found; however, slight changes were observed. First, the incorporation of TiO$_2$ tends to shift the band assigned to the stretching of hydroxyl and amine groups to higher wavenumbers, reaching approximately 3283 cm^{-1}. In contrast, the opposite effect was observed for C—O bonds, which shifted to lower wavenumbers, reaching a maximum intensity at 1038 cm^{-1}. Moreover, it is important to note that the band assigned to the amide II vibration shows a considerable decrease in intensity and a shift to higher wavenumbers at 1558 cm^{-1}. Additionally, a similar slight blueshift was also observed for the amide I vibrational mode, reaching 1651 cm^{-1}. Similar results were also observed for the nanocomposites containing AuTiO$_2$ and CuAuTiO$_2$, which might indicate the relevant participation of these
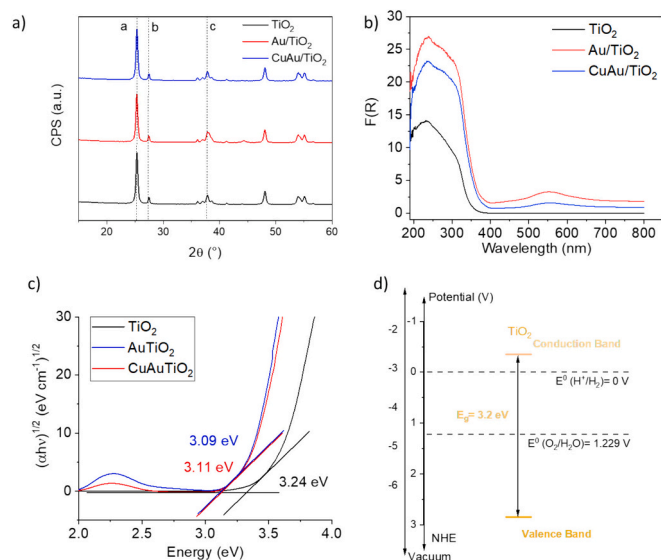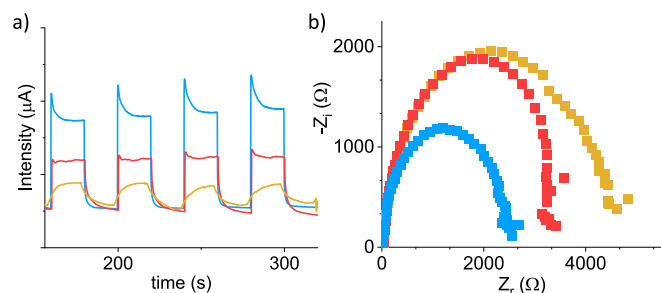
Fig. 4. (a) XRD diffractograms, (b) DRS spectra, (c) Tauc plots and (d) energy band level diagram of TiO$_2$ P25 NPs and the redox potentials for water splitting reactions.

Table 1
Summary of the phase composition and average crystallite diameter for the different nanocomposites.

Sample	%A	%R	d (nm)	
			Anatase	Rutile
TiO$_2$	86.7	13.3	20.2	27.8
1 % AuTiO$_2$	86.5	13.5	20.0	24.4
1 % CuAuTiO$_2$	86.0	14.0	19.9	23.9

Fig. 5. (a) Transient photocurrent responses and (b) Nyquist plots of CuAuTiO$_2$ (blue), AuTiO$_2$ (red), and TiO$_2$ (yellow).

functional groups, mainly amines, hydroxyls and carbonyls, in interacting with the surface of the incorporated NPs to achieve dispersion in the material; these results have been addressed by Li et al. [59] and Chrissafis et al. [60] for the stabilization of CdS quantum dots and SiO$_2$ nanoparticles with chitosan, respectively. Similarly, Chen and coworkers discussed the blueshift of amine vibrations in terms of the strong interaction between amine lone pairs by hydrogen bonding interactions [61]. In this sense, the interaction mode could be expanded to include chitosan hydroxyls, amines and amides with the surface of the hydroxyl functional groups of TiO$_2$, serving as anchor groups to retain and stabilize the NPs. In addition, the presence of Au and CuAu NPs on TiO$_2$ could serve as important points for interaction with chitosan functional groups, in which the participation of the hydrophilic functional groups of chitosan with these kinds of nanostructures has been previously explored by the DSC technique, revealing important consequences for the amount of freezable water inside hydrogels by the

introduction of these kinds of NPs [62]. In addition, the observed shifts in the vibrational modes of the chitosan functional groups might also be correlated with the changes observed in the T$_{md}$ obtained for the nanocomposites. In this context, strong interactions between dispersants and stabilizing groups such as hydroxyl, amine, or amide groups could decrease the bond strength of chitosan main chain bonds, as observed in the redshifts in the C—O and C—O—C vibrational modes, which translates to a decrease in the bond strength of the glycosidic main chain, affecting the thermal stability of the nanocomposite.

Later, the hydrogel nanocomposites were evaluated as photocatalysts for the HER under both visible and simulated sunlight irradiation, Fig. 7. Based on previous reports, it is likely that the reaction proceeds via several reaction steps that involve several elementary steps, such as the photogeneration of charge carriers (Eq. (1)), the reduction of protons (Eq. (2)) and the oxidation of hole-scavenging species such as methanol (Eq. (3)) [63,64].

$$TiO_2 + h\upsilon \rightarrow h^+ + e^- \tag{1}$$

$$2H^+_{(ads)} + 2e^- \rightarrow H_{2\ (g)} \tag{2}$$

$$CH_3OH_{(ads)} + h^+ \rightarrow CH_3OH^{\cdot}_{(ads)} + H^+ \tag{3}$$

To conduct the photocatalytic reactions, certain amounts of lyophilized samples were immersed in a methanol–water mixture inside a glass reactor and tested using different light filters. In this scenario, methanol acts as a hole scavenger for the photogenerated holes in the semiconductor, increasing the lifetime of the photogenerated electrons and favoring the proton reduction reaction to H$_2$ [65,66]. Fig. 7 summarizes the obtained hydrogen production rates using the series of photocatalysts under simulated sunlight or visible light irradiation. As can be observed, AuTiO$_2$ and CuAuTiO$_2$ loaded into ChTPP beads were more photocatalytic active than TiO$_2$/ChTPP, results that reveals similar hydrogen production rates trends to the one demonstrated by NPs in absence of the hydrogel support, SI 14. Control experiments revealed that in the absence of photocatalyst or in the presence of ChTPP beads without TiO$_2$ immersed in the reaction medium, hydrogen was not generated. This order of photocatalytic activity agrees with the efficiency of photoinduced charge separation achieved by CuAuTiO$_2$/ChTPP, AuTiO$_2$/ChTPP and TiO$_2$/ChTPP, as evidenced by the transient photocurrent and Nyquist plots. In a control experiment using TiO$_2$ suspended in water in the absence of and in the presence of dissolved chitosan revealed a photocatalytic hydrogen production of 38.55 or 119.38 μmol g^{-1} h^{-1}, respectively, a fact that agree with the role of chitosan as hole-scavenger species. To gain more information about the photoinduced charge separation and reaction mechanism during the HER, an analogous photocatalytic experiment using CuAuTiO$_2$/ChTPP but using only water as reaction medium was conducted. The obtained results showed that hydrogen generation using pure water is lower (263 μmol g^{-1} h^{-1}) than that achieved when using a water:methanol mixture (1790 μmol g^{-1} h^{-1}). This data reinforces the photocatalytic reaction mechanism in where irradiation of the photocatalyst results in the formation of electrons and holes. Photogenerated electrons are responsible of proton reduction reaction to hydrogen while photogenerated holes responsible of water or methanol oxidation. The lower photocatalytic hydrogen generation when using pure water agrees with the fact that water oxidation to oxygen a more kinetically and thermodynamically demanding half-reaction compared to methanol oxidation [67].

In good agreement with the optical properties of TiO$_2$/ChTPP, this solid exhibited negligible photocatalytic activity under visible light irradiation ($\lambda > 420$ nm). Importantly, AuTiO$_2$/ChTPP and, in particular, CuAuTiO$_2$/ChTPP are active under these conditions. Interestingly, even though CuAuTiO$_2$/ChTPP has a lower cocatalyst content (0.8 mol% with respect to TiO$_2$) than does AuTiO$_2$/ChTPP (1.2 mol% with respect to TiO$_2$), the former exhibits higher activity. The higher activity of CuAuTiO$_2$/ChTPP can be attributed to the presence of relatively small
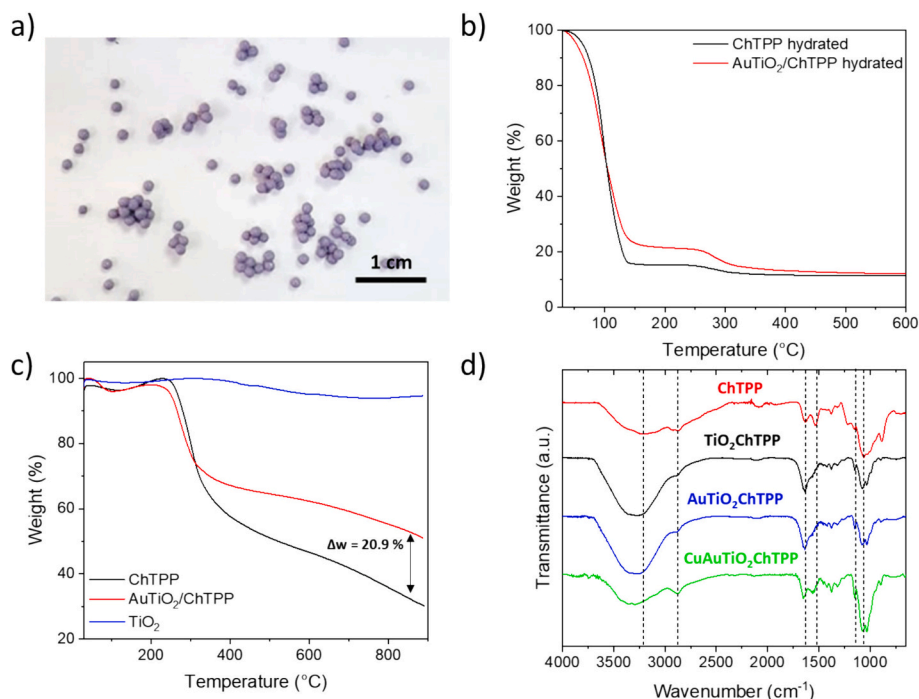
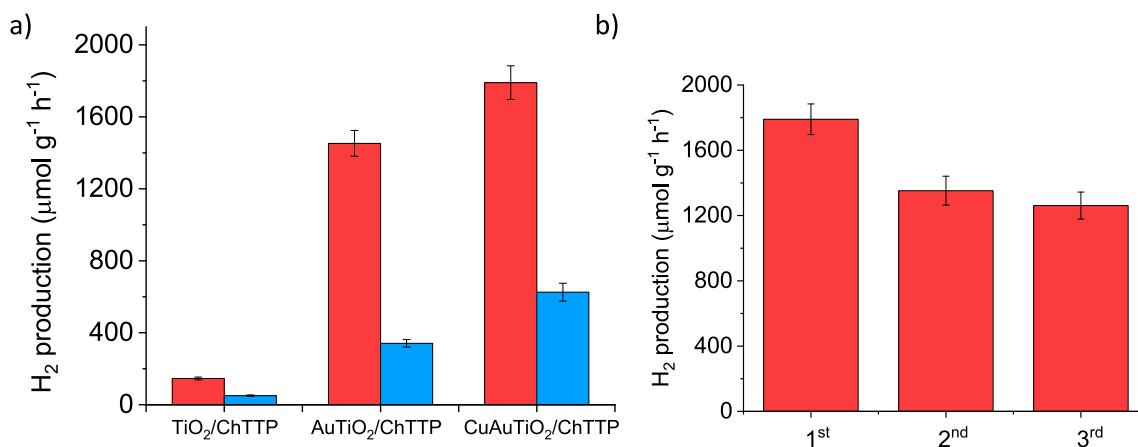**Fig. 6.** (a) Digital image, (b) TGA of wet hydrogel samples, (c) lyophilized samples, and (d) FT–IR spectra.

Fig. 7. (a) Photocatalytic hydrogen generation profiles of TiO_2/ChTPP, $AuTiO_2$/ChTPP and $CuAuTiO_2$/ChTPP using AM 1.5G and 420 nm cutoff filters. (b) Hydrogen generation recyclability tests using the $CuAuTiO_2$/ChTPP nanocomposite under simulated solar irradiation with an AM 1.5G filter.

bimetallic alloyed CuAu NPs compared to that of $AuTiO_2$/ChTPP. A similar result was previously reported by Yu and coworkers, who observed the remarkable synergy of CuAu bimetallic nanostructures deposited on semiconducting materials, which were employed for the photoreduction of CO_2 into value-added products [68]. Based on the authors' findings, the increase in which Cu atoms on the catalysts improve not only the photoreduction of CO_2 but also the generation of hydrogen could be associated with the better capacity of Cu atoms to act as active sites to perform the reduction reaction when combined with Au atoms.

Under both solar-simulated and visible-light irradiation conditions, catalysts loaded with $MTiO_2$ demonstrated a considerably enhanced hydrogen production performance against pristine TiO_2 encapsulated inside the hydrogels. In addition, under simulated solar conditions, the catalyst demonstrated a considerable enhancement over that of the hydrogels loaded with TiO_2, which was also remarkably greater than that observed under visible light irradiation conditions. The observed

behavior of the catalysts could be attributed to different factors; in fact, the observed tendency under visible light conditions could be mostly attributed to the increase in the absorption window of the material into the visible region, as observed during the characterization of the optical properties of the different materials, allowing an improved absorption of photons to excite electrons from TiO_2, which latterly conducts the HER [69]. On the other hand, under simulated solar conditions, with a slight presence of UV radiation, the catalyst exhibited considerably greater performance, in which the advantage observed under visible light irradiation was added to a decrease in the recombination rate of photogenerated species, improving the lifetime of photogenerated electrons to conduct the reduction reaction. This effect has been previously described in the literature by the formation of a Schottky barrier at the metal–semiconductor interface, promoting an electron trapping mechanism [63,70]. This is in agreement with our findings, in which transient photocurrent and Nyquist plots demonstrate the enhanced capability of decorated semiconductors to photogenerate and to transfer them in

order to carry the HER.

Given the noteworthy activity of the hydrogels loaded with CuAu-TiO$_2$, recyclability assays were subsequently conducted to test the stability of the nanocomposite during several catalytic cycles. The hydrogen production rates obtained in each cycle are depicted in Fig. 7b. The catalyst was able to continuously generate hydrogen over the evaluated cycles, reaching rates of 1790 μmol g^{-1} h^{-1} in its first cycle, with a slight decrease in the subsequent cycles, obtaining average production rates of 1354 and 1263 μmol g^{-1} h^{-1} in the second and third cycles, respectively. This demonstrates mild activity from the material after continuous irradiation lapses, which is comparable to the results reported by Mondal et al. [71], who observed a decrease in the catalytic activity of Cu/CuO@TiO$_2$ during recyclability experiments, which was mainly attributed to a disruption of the interaction between the cocatalyst (Cu/CuO) and the semiconductor, mostly related to the long periods of irradiation, an effect that could explain the observed result by our nanocomposites. Additionally, the stability of CuAuTiO$_2$/ChTPP after three consecutive uses was assessed by XRD, SI 15, and ICP-OES measurements, SI 16. The obtained results indicate that the crystallinity of the sample is preserved after the photocatalytic uses while a small metal leaching from the solid to the solution was observed in the case of Cu (1.75 wt%) and in less extent for Au (0.065 wt%) or Ti (0.023 wt%) elements.

Finally, the nanocomposites were compared against other photocatalytic nanocomposites reported in the literature, as shown in Table 2. However, it is noteworthy that it is difficult to compare materials, given the wide diversity of systems and setups employed to test the activity of the material, such as the variability of lamps, irradiation intensities, filters, reaction media and metallic load, just to name a few [72]; however, these factors were considered to provide a more accurate description of the material for comparison. Despite the above, according to the results obtained for the nanocomposites synthesized in this study, AuTiO$_2$/ChTPP and CuAuTiO$_2$/ChTPP exhibited adequate activity compared with semiconducting materials decorated with only noble metals, such as those used by Méndez et al. [72] with a hydrogen production rate of approximately 2336 μmol g^{-1} h^{-1} by using TiO$_2$ decorated with Au NPs together with other metallic elements, such as Pt, Pd and Ag; the introduction of Pt helped to reduce the recombination of photoexcited species, improving the half lifetime of these species to reduce water molecules. Nevertheless, those systems presented a metallic decoration of approximately 0.5 % *w/w*, which is above the value employed in this work and could explain the higher catalytic performance reported by the authors. In addition, the poor photocatalytic activity of TiO$_2$ and Pt/TiO$_2$ for the generation of hydrogen under similar irradiation conditions was also reported (~one sun with an AM 1.5G filter), in which no hydrogen evolution was detected.

4. Conclusions

A biobased nanocomposite capable of driving the photocatalytic production of hydrogen under simulated sunlight irradiation was obtained in this work. The material consisted of decorated TiO$_2$ with low amounts of Au and Cu NPs, 1.2 and 0.8 mol% for the Au- and CuAu-decorated systems, respectively, as evidenced by ICP–OES and further characterized by several techniques, such as HR–TEM, FE–SEM and EDX. Characterization of Au- or CuAu NP-supported TiO$_2$ revealed that these solids exhibit a lower band gap than pristine TiO$_2$, enabling visible light absorption associated with the LSPR absorption of Au and Cu nanostructures. Importantly, compared with TiO$_2$, AuTiO$_2$ and, especially, CuAuTiO$_2$ exhibited greater photoinduced charge separation efficiencies based on their transient photocurrent response and Nyquist plots. After the incorporation of the decorated NPs into the hydrogels, slight changes in the thermal properties of the nanocomposites and shifts in the vibrational modes of the chitosan functional groups were observed. These results helped to support important interactions between chitosan functional groups, mainly hydroxyl, amine, and amide groups, and the surface of TiO$_2$ to achieve stabilization and proper encapsulation inside the hydrogel structure. Finally, the nanocomposites were tested for photocatalytic HER using water and methanol mixtures under simulated sunlight irradiation. CuAuTiO$_2$/ChTPP exhibited the highest activity (1790 μmol g^{-1} h^{-1}), followed by AuTiO$_2$/ChTPP (1402 μmol g^{-1} h^{-1}), and finally, the pristine TiO$_2$/ChTPP results agreed with the relative efficiencies of charge separation for these MTiO$_2$ solids. Furthermore, Au and CuAu NP-supported TiO$_2$ were also found to be active under visible light irradiation (λ > 420 nm) and associated with the LSPR of these NPs. These results serve as interesting preambles for the use of biopolymers in photocatalytic hydrogen generation technologies. Hazard concerns of the material, mostly safe product to be employed.

CRediT authorship contribution statement

Oscar Ramírez: Writing – review & editing, Writing – original draft, Methodology, Investigation, Conceptualization. **Antón Lopéz-Frances:** Writing – review & editing, Investigation. **Herme G. Baldoví:** Writing – review & editing, Investigation. **César Saldías:** Writing – review & editing, Supervision, Conceptualization. **Sergio Navalón:** Writing – review & editing, Methodology, Formal analysis. **Angel Leiva:** Writing – review & editing, Supervision, Funding acquisition, Conceptualization. **David Díaz Díaz:** Writing – review & editing, Supervision, Methodology, Formal analysis, Conceptualization.

Table 2

A comparison of the hydrogen production rate with that of other photocatalysts can be found in the literature.

Sample	Metal (% *w/w*)	Irradiating source	Irradiation window	Hole scavengers (% *v/v*)	r_H (μmol g$_{cat}^{-1}$ h^{-1})	Reference
Au/TiO$_2$	0.5	Xe 450 W	345–575 nm	Methanol (50)	2336	[72]
Ag/TiO$_2$	0.5	Xe 450 W	345–575 nm	Methanol (50)	716	[72]
Au/TiO$_2$	1	Solar Simulation 300 W	Filter AM1.5	Methanol (25)	307	[73]
PtAu/TiO$_2$	1[a] – 1[b]	Solar Simulation 300 W	Filter AM1.5	Methanol (25)	1091	[73]
AgAu/TiO$_2$	1[b] – 0.5[c]	Solar Simulation 300 W	Filter AM1.5	Methanol (25)	466	[73]
Pt/TiO$_2$	0.5	Purple Lamp 13 W	250–400 nm (52 %) 400–700 nm (48 %)	Methtanol (50)	349	[74]
Pt/CXB@CdS	0.1	Xe 300 W	λ > 420 nm	Na$_2$S (0.35 M) Na$_2$SO$_3$ (0.25 M)	287	[75]
NFC@Fe$_3$O$_4$@TNP	–	Xe 300 W	300 nm	Methanol (20)	436	[76]
AS/NTO/CS	0.1[a] – 17.5[c]	Xe 300 W	No filter	Triethanolamine	62	[77]
AuTiO$_2$/ChTPP	1.2[d]	Hg-Xe 150 W	Filter AM1.5G	Methanol (10)	1402	This work
CuAuTiO$_2$/ChTPP	0.8[d]	Hg-Xe 150 W	Filter AM1.5G	Methanol (10)	1790	This work

[a] w/w percentage of Pt deposited on the semiconducting material.
[b] w/w percentage of Au deposited on the semiconducting material.
[c] w/w percentage of Ag deposited on the semiconducting material.
[d] mol percentage of metals deposited on the semiconducting material.

Declaration of competing interest

The authors declare that they have no known competing financial interests or personal relationships that could have appeared to influence the work reported in this paper.

Data availability

Data will be made available on request.

Acknowledgments

Appendix A. Supplementary data

Supplementary data to this article can be found online at https://doi.org/10.1016/j.ijbiomac.2024.132898.

References

[1] M.J. Pickl, The renewable energy strategies of oil majors–from oil to energy? Energ. Strat. Rev. 26 (2019) 100370.
[2] J. Xu, M. Akhtar, M. Haris, S. Muhammad, O.J. Abban, F. Taghizadeh-Hesary, Energy crisis, firm profitability, and productivity: an emerging economy perspective, Energ. Strat. Rev. 41 (2022) 100849.
[3] A.S. Al-Ezzi, M.N.M. Ansari, Photovoltaic solar cells: a review, Applied System Innovation 5 (4) (2022) 67.
[4] M. Kroff, S.A. Hevia, J.N. O`Shea, I.G.d. Muro, V. Palomares, T. Rojo, R. del Río, Lithium Iron phosphate/carbon (LFP/C) composite using nanocellulose as a reducing agent and carbon source, Polymers 15 (12) (2023) 2628.
[5] L. Fan, Z. Tu, S.H. Chan, Recent development of hydrogen and fuel cell technologies: a review, Energy Rep. 7 (2021) 8421–8446.
[6] I. Jain, Hydrogen the fuel for 21st century, Int. J. Hydrog. Energy 34 (17) (2009) 7368–7378.
[7] M.A. Haider, N.D. Chaturvedi, An energy-efficient and cleaner production of hydrogen by steam reforming of glycerol using Aspen Plus, Int. J. Hydrog. Energy 49 (Part C) (2 January 2024) 1311–1320.
[8] Z. Navas-Anguita, D. García-Gusano, J. Dufour, D. Iribarren, Revisiting the role of steam methane reforming with CO2 capture and storage for long-term hydrogen production, Sci. Total Environ. 771 (2021) 145432.
[9] A. Fujishima, K.J.n. Honda, Electrochemical photolysis of water at a semiconductor electrode, Nature 238 (5358) (1972) 37–38.
[10] S. Nishioka, F.E. Osterloh, X. Wang, T.E. Mallouk, K. Maeda, Photocatalytic water splitting, Nature Reviews Methods Primers 3 (1) (2023) 42.
[11] L. Lin, T. Hisatomi, S. Chen, T. Takata, K.J.T.i.C. Domen, Visible-light-driven photocatalytic water splitting: recent progress and challenges 2 (9) (2020) 813–824.
[12] K.H. Ng, S.Y. Lai, C.K. Cheng, Y.W. Cheng, C.C. Chong, Photocatalytic water splitting for solving energy crisis: myth, fact or busted? Chem. Eng. J. 417 (2021) 128847.
[13] J. Herman, R. McKenzie, S. Diaz, J. Kerr, S. Madronich, G. Seckmeyer, Ultraviolet Radiation at the Earth's Surface, UMBC Joint Center for Earth Systems Technology, 2023.
[14] G. Pahlevanpour, H. Bashiri, Kinetic Monte Carlo simulation of hydrogen production from photocatalytic water splitting in the presence of methanol by 1 wt % Au/TiO2, Int. J. Hydrog. Energy 47 (26) (2022) 12975–12987.
[15] J. Krýsa, G. Waldner, H. Mĕšťánková, J. Jirkovský, G. Grabner, Photocatalytic degradation of model organic pollutants on an immobilized particulate TiO2 layer: roles of adsorption processes and mechanistic complexity, Appl. Catal. B Environ. 64 (3–4) (2006) 290–301.
[16] E. Antolini, Photo-assisted methanol oxidation on Pt-TiO2 catalysts for direct methanol fuel cells: a short review, Appl. Catal. B Environ. 237 (2018) 491–503.
[17] W. Liang, X. Du, Y. Zhu, S. Ren, J. Li, Catalytic oxidation of chlorobenzene over Pd-TiO2/Pd-Ce/TiO2 catalysts, Catalysts 10 (3) (2020) 347.
[18] K. Omri, N. Alonizan, R.A. Abumousa, M. Alqahtani, T. Ghrib, Fabrication and enhanced UV-light photocatalytic performance of Mn2O3/Dy2O3 nanocomposites 34 (5) (2023) 432.
[19] M. Madani, H. Mansour, K. Omri, N. Alonizan, S. Gouadria, L. El Mir, A novel route to the synthesis of CdS/α-Fe2O3 nanocomposite for enhanced photocatalytic performance 138 (8) (2023) 720.
[20] T.C.M.V. Do, D.Q. Nguyen, K.T. Nguyen, P.H. Le, TiO2 and Au-TiO2 nanomaterials for rapid photocatalytic degradation of antibiotic residues in aquaculture wastewater, Materials 12 (15) (2019) 2434.
[21] D. Kanakaraju, F.D. anak Kutiang, Y.C. Lim, P.S. Goh, Recent progress of Ag/TiO2 photocatalyst for wastewater treatment: doping, co-doping, and green materials functionalization, Appl. Mater. Today 27 (2022) 101500.
[22] C. Wei, Q. Liu, Shape-, size-, and density-tunable synthesis and optical properties of copper nanoparticles, CrystEngComm 19 (24) (2017) 3254–3262.
[23] P. Liu, H. Wang, X. Li, M. Rui, H. Zeng, Localized surface plasmon resonance of Cu nanoparticles by laser ablation in liquid media, RSC Adv. 5 (97) (2015) 79738–79745.
[24] M. Dhonde, K. Sahu, V. Murty, S.S. Nemala, P. Bhargava, Surface plasmon resonance effect of Cu nanoparticles in a dye sensitized solar cell, Electrochim. Acta 249 (2017) 89–95.
[25] C. Lee, N.R. Kim, J. Koo, Y.J. Lee, H.M. Lee, Cu-Ag core–shell nanoparticles with enhanced oxidation stability for printed electronics, Nanotechnology 26 (45) (2015) 455601.
[26] L. Chen, J. Lei, L. Tian, K. Lv, S. Jin, Schottky construction of bimetallic Au-Cu alloy@ TiO2 hollow nanoboxes embedded optical switch for enhancing photocatalytic and selective adsorption activities via one-pot deposition-precipitation strategy, J. Alloys Compd. 943 (2023) 168978.
[27] C.L. Bracey, P.R. Ellis, G.J. Hutchings, Application of copper–gold alloys in catalysis: current status and future perspectives 38 (8) (2009) 2231–2243.
[28] R. Kavitha, S.G.J.C.P. Kumar, Review on bimetallic-deposited TiO2: preparation methods, charge carrier transfer pathways and photocatalytic applications 74 (3) (2020) 717–756.
[29] A. Guesmi, M.M. Cherif, O. Baaloudj, H. Kenfoud, A.K. Badawi, W. Elfalleh, N. B. Hamadi, L. Khezami, A.A. Assadi, Disinfection of corona and myriad viruses in water by non-thermal plasma: a review, Environ. Sci. Pollut. Res. 29 (37) (2022) 55321–55335.
[30] O. Baaloudj, N. Nasrallah, H. Kenfoud, K.W. Bourkeb, A.K. Badawi, Polyaniline/ Bi12TiO20 hybrid system for cefixime removal by combining adsorption and photocatalytic degradation, ChemEngineering 7 (1) (2023) 4.
[31] B.-J. Hsieh, M.-C. Tsai, C.-J. Pan, W.-N. Su, J. Rick, H.-L. Chou, J.-F. Lee, B.-J. Hwang, Tuning metal support interactions enhances the activity and durability of TiO2-supported Pt nanocatalysts, Electrochim. Acta 224 (2017) 452–459.
[32] P. Petzoldt, M. Eder, S. Mackewicz, M. Blum, T. Kratky, S. Günther, M. Tschurl, U. Heiz, B.A. Lechner, Tuning strong metal–support interaction kinetics on Pt-loaded TiO2 (110) by choosing the pressure: a combined ultrahigh vacuum/near-ambient pressure XPS study, J. Phys. Chem. C 126 (38) (2022) 16127–16139.
[33] L. Wang, Y. Zhang, L. Chen, H. Xu, Y. Xiong, 2D polymers as emerging materials for photocatalytic overall water splitting, Adv. Mater. 30 (48) (2018) 1801955.
[34] C. Zhao, Z. Chen, R. Shi, X. Yang, T. Zhang, Recent advances in conjugated polymers for visible-light-driven water splitting, Adv. Mater. 32 (28) (2020) 1907296.
[35] P. Guiglion, C. Butchosa, M.A. Zwijnenburg, Polymer photocatalysts for water splitting: insights from computational modeling, Macromol. Chem. Phys. 217 (3) (2016) 344–353.
[36] V. Tournier, S. Duquesne, F. Guillamot, H. Cramail, D. Taton, A. Marty, I. André, Enzymes' power for plastics degradation, Chem. Rev. 123 (9) (2023) 5612–5701.
[37] T.J.M.T.P. Biswal, Biopolymers for tissue engineering applications: a review 41 (2021) 397–402.
[38] S.K. Juikar, S.G. Warkar, Biopolymers for packaging applications: an overview, Packag. Technol. Sci. 36 (4) (2023) 229–251.
[39] M.M. Abo Elsoud, E. El Kady, Current trends in fungal biosynthesis of chitin and chitosan, Bull. Natl. Res. Cent. 43 (1) (2019) 1–12.
[40] A.K. Badawi, R.S. Salama, M.M.M. Mostafa, Natural-based coagulants/flocculants as sustainable market-valued products for industrial wastewater treatment: a review of recent developments, RSC Adv. 13 (28) (2023) 19335–19355.
[41] A.K. Badawi, B. Ismail, O. Baaloudj, K.Z. Abdalla, Advanced wastewater treatment process using algal photo-bioreactor associated with dissolved-air flotation system: a pilot-scale demonstration 46 (2022) 102565.
[42] H. Amiri, M. Aghbashlo, M. Sharma, J. Gaffey, L. Manning, S.M. Moosavi Basri, J. F. Kennedy, V.K. Gupta, M. Tabatabaei, Chitin and chitosan derived from crustacean waste valorization streams can support food systems and the UN Sustainable Development Goals, Nature Food 3 (10) (2022) 822–828.
[43] B. Gupta, A.K. Gupta, Photocatalytic performance of 3D engineered chitosan hydrogels embedded with sulfur-doped C3N4/ZnO nanoparticles for ciprofloxacin removal: degradation and mechanistic pathways, Int. J. Biol. Macromol. 198 (2022) 87–100.
[44] K. Karthikeyan, A. Nithya, K. Jothivenkatachalam, Photocatalytic and antimicrobial activities of chitosan-TiO2 nanocomposite, Int. J. Biol. Macromol. 104 (2017) 1762–1773.
[45] A. Sengeni, S. Noda, Prior oxidation of Ni substrates increases the number of active sites in Ni3S2 obtained by sulfidation and enhances its multifunctional electrocatalytic activity, J. Mater. Chem. A 12 (2024) 5793–5804.
[46] S.F. Chen, J.P. Li, K. Qian, W.P. Xu, Y. Lu, W.X. Huang, S.H. Yu, Large scale photochemical synthesis of M@ TiO2 nanocomposites (M= Ag, Pd, Au, Pt) and their optical properties, CO oxidation performance, and antibacterial effect, Nano Res. 3 (2010) 244–255.

[47] M. Cabrero-Antonino, B. Ferrer, H.G. Baldoví, S. Navalón, Toward solar-driven photocatalytic CO2 methanation under continuous flow operation using benchmark MIL-125 (Ti)–NH2 supported ruthenium nanoparticles, Chem. Eng. J. 445 (2022) 136426.

[48] C.M. Rueda-Navarro, M. Cabrero-Antonino, P. Escamilla, V. Díez-Cabanes, D. Fan, P. Atienzar, B. Ferrer, I. Vayá, G. Maurin, H.G. Baldoví, Solar-assisted photocatalytic water splitting using defective UiO-66 solids from modulated synthesis, Nano Res. (2023) 1–17.

[49] F. Lakadamyali, A. Reynal, M. Kato, J.R. Durrant, E. Reisner, Electron transfer in dye-sensitised semiconductors modified with molecular cobalt catalysts: photoreduction of aqueous protons, Chem Eur J 18 (48) (2012) 15464–15475.

[50] L.X. Chen, T. Rajh, Z. Wang, M.C. Thurnauer, XAFS studies of surface structures of TiO2 nanoparticles and photocatalytic reduction of metal ions, J. Phys. Chem. B 101 (50) (1997) 10688–10697.

[51] J. Ding, X. Li, L. Chen, X. Zhang, X. Tian, Photocatalytic hydrogen production over plasmonic AuCu/CaIn2S4 composites with different AuCu atomic arrangements, Appl. Catal. B Environ. 224 (2018) 322–329.

[52] R.A. Spurr, H. Myers, Quantitative analysis of anatase-rutile mixtures with an X-ray diffractometer, Anal. Chem. 29 (5) (1957) 760–762.

[53] P. Makuła, M. Pacia, W. Macyk, How to correctly determine the band gap energy of modified semiconductor photocatalysts based on UV–Vis spectra, The Journal of Physical Chemistry Letters 9 (23) (2018) 6814–6817.

[54] J.D. Giraldo, V.H. Campos-Requena, B.L. Rivas, Chitosan–tripolyphosphate bead: the interactions that govern its formation, Polym. Bull. 76 (2019) 3879–3903.

[55] D. de Britto, S.P. Campana-Filho, Kinetics of the thermal degradation of chitosan, Thermochim. Acta 465 (1–2) (2007) 73–82.

[56] I. Corazzari, R. Nisticò, F. Turci, M.G. Faga, F. Franzoso, S. Tabasso, G. Magnacca, Advanced physico-chemical characterization of chitosan by means of TGA coupled on-line with FTIR and GCMS: thermal degradation and water adsorption capacity, Polym. Degrad. Stab. 112 (2015) 1–9.

[57] L. Xiao, B. Pang, Experimental study on the effect of calcination on the volcanic ash activity of diatomite, in: IOP Conference Series: Materials Science and Engineering, IOP Publishing, 2017, p. 012089.

[58] J. Zawadzki, H. Kaczmarek, Thermal treatment of chitosan in various conditions, Carbohydr. Polym. 80 (2) (2010) 394–400.

[59] Z. Li, Y. Du, Z. Zhang, D. Pang, Preparation and characterization of CdS quantum dots chitosan biocomposite, React. Funct. Polym. 55 (1) (2003) 35–43.

[60] K. Chrissafis, K.M. Paraskevopoulos, G.Z. Papageorgiou, D.N. Bikiaris, Thermal and dynamic mechanical behavior of bionanocomposites: fumed silica nanoparticles dispersed in poly (vinyl pyrrolidone), chitosan, and poly (vinyl alcohol), J. Appl. Polym. Sci. 110 (3) (2008) 1739–1749.

[61] Y. Chen, X. Liu, S. Braun, M. Fahlman, Understanding Interface dipoles at an electron transport material/electrode modifier for organic electronics, ACS Appl. Mater. Interfaces 13 (39) (2021) 47218–47225.

[62] O. Ramírez, S. Castillo, S. Bonardd, C. Saldías, J.N. O'Shea, C.P.C. Ryder, D.D. Díaz, A. Leiva, Marrying plasmonic earth-abundant metals with catalytic metals for visible-light-promoted hydrogen generation on biobased materials, J. Environ. Chem. Eng. 11 (5) (2023) 111036.

[63] V. Kumaravel, S. Mathew, J. Bartlett, S.C. Pillai, Photocatalytic hydrogen production using metal doped TiO2: a review of recent advances, Appl. Catal. B Environ. 244 (2019) 1021–1064.

[64] J. Castillo-Rodríguez, P.D. Ortiz, M. Isaacs, N.P. Martinez, J.N. O'Shea, J. Hart, R. Temperton, X. Zarate, D. Contreras, E. Schott, Highly efficient hydrogen evolution reaction, plasmon-enhanced by AuNP-l-TiO 2 NP photocatalysts, New J. Chem. 44 (38) (2020) 16491–16500.

[65] A. Presciutti, F. Asdrubali, A. Marrocchi, A. Broggi, G. Pizzoli, A. Damiani, Sun simulators: development of an innovative low cost film filter, Sustainability 6 (10) (2014) 6830–6846.

[66] V. Esen, Ş. Sağlam, B. Oral, Light sources of solar simulators for photovoltaic devices: a review, Renew. Sustain. Energy Rev. (2017) 1240–1250.

[67] S. Navalón, A. Dhakshinamoorthy, M. Álvaro, B. Ferrer, H. García, Metal–organic frameworks as photocatalysts for solar-driven overall water splitting, Chem. Rev. 123 (1) (2022) 445–490.

[68] Y. Yu, X.a. Dong, P. Chen, Q. Geng, H. Wang, J. Li, Y. Zhou, F. Dong, Synergistic effect of Cu single atoms and Au–Cu alloy nanoparticles on TiO2 for efficient CO2 photoreduction, ACS Nano 15 (9) (2021) 14453–14464.

[69] F. Wang, R.J. Wong, J.H. Ho, Y. Jiang, R. Amal, Sensitization of Pt/TiO2 using plasmonic Au nanoparticles for hydrogen evolution under visible-light irradiation, ACS Appl. Mater. Interfaces 9 (36) (2017) 30575–30582.

[70] M.J. Rivero, O. Iglesias, P. Ribao, I. Ortiz, Kinetic performance of TiO2/Pt/reduced graphene oxide composites in the photocatalytic hydrogen production, Int. J. Hydrog. Energy 44 (1) (2019) 101–109.

[71] I. Mondal, U. Pal, Synthesis of MOF templated Cu/CuO@ TiO 2 nanocomposites for synergistic hydrogen production, Phys. Chem. Chem. Phys. 18 (6) (2016) 4780–4788.

[72] F.J. Méndez, A. González-Millán, J.A. García-Macedo, Surface modification of titanium oxide as efficient support of metal nanoparticles for hydrogen production via water splitting, Mater. Chem. Phys. 232 (2019) 331–338.

[73] A.A. Melvin, K. Illath, T. Das, T. Raja, S. Bhattacharyya, C.S. Gopinath, M–Au/TiO 2 (M=Ag, Pd, and Pt) nanophotocatalyst for overall solar water splitting: role of interfaces, Nanoscale 7 (32) (2015) 13477–13488.

[74] F.J. Méndez, D. Barrón-Romero, O. Pérez, R.D. Flores-Cruz, Y. Rojas-Challa, J. A. García-Macedo, A highly efficient and recyclable Pt/TiO2 thin film photocatalytic system for sustainable hydrogen production, Mater. Chem. Phys. 305 (2023) 127925.

[75] Y. Zhang, W. Zhou, L. Jia, X. Tan, Y. Chen, Q. Huang, B. Shao, T. Yu, Visible light driven hydrogen evolution using external and confined CdS: effect of chitosan on carriers separation, Appl. Catal. B Environ. 277 (2020) 119152.

[76] X. An, D. Cheng, L. Dai, B. Wang, H.J. Ocampo, J. Nasrallah, X. Jia, J. Zou, Y. Long, Y. Ni, Synthesis of nano-fibrillated cellulose/magnetite/titanium dioxide (NFC@ Fe3O4@ TNP) nanocomposites and their application in the photocatalytic hydrogen generation, Appl. Catal. B Environ. 206 (2017) 53–64.

[77] J. Wang, J. Sun, J. Huang, A. Fakhri, V.K.J.M.C. Gupta, Physics, synthesis and its characterization of silver sulfide/nickel titanate/chitosan nanocomposites for photocatalysis and water splitting under visible light, and antibacterial studies, Mater. Chem. Phys. 272 (2021) 124990.